

Characterization of interlayer coupling in YIG/Py bilayer using polarized neutron reflectometry

He Bai(白鹤), Wei He(何为), Dan Liu(刘丹), Jialiang Li(李嘉亮), Xiao Deng(邓霄), Yuan Sun(孙远), Songwen Xiao(肖松文), Sheng Cheng(成晟), Xiaozhi Zhan(詹晓芝), Jianwang Cai(蔡建旺), and Tao Zhu(朱涛)
Citation: Chin. Phys. B, 2025, 34 (**10**): 107509. DOI: 10.1088/1674-1056/adf31e
http://cpb.iphy.ac.cn; http://iopscience.iop.org/cpb

What follows is a list of articles you may be interested in

Perpendicular magnetic anisotropy of Pd/Co_2MnSi/Co/Pd multilayer

Xiaoqi Qin(秦晓奇), Jiaxing Tan(谭家兴), Xianwu Xiu(修显武), Wentian Cao(曹文田), and Shuyun Wang(王书运)
Chin. Phys. B, 2025, 34 (**3**): 037502. DOI: 10.1088/1674-1056/ada694

Magnon bands in twisted bilayer honeycomb quantum magnets

Xingchuan Zhu(朱兴川), Huaiming Guo(郭怀明), and Shiping Feng(冯世平)
Chin. Phys. B, 2021, 30 (**7**): 077505. DOI: 10.1088/1674-1056/abeee5

Emergent O(4) symmetry at the phase transition from plaquette-singlet to antiferromagnetic order in quasi-two-dimensional quantum magnets

Guangyu Sun(孙光宇), Nvsen Ma(马女森), Bowen Zhao(赵博文), Anders W. Sandvik, and Zi Yang Meng(孟子杨)
Chin. Phys. B, 2021, 30 (**6**): 067505. DOI: 10.1088/1674-1056/abf3b8

Antiferromagnetic interlayer coupling of (111)-oriented $La_{0.67}Sr_{0.33}MnO_3$/$SrRuO_3$ superlattices

Hui Zhang(张慧), Jing Zhang(张静), Jin-E Zhang(张金娥), Fu-Rong Han(韩福荣), Hai-Lin Huang(黄海林), Jing-Hua Song(宋京华), Bao-Gen Shen(沈保根), Ji-Rong Sun(孙继荣)
Chin. Phys. B, 2019, 28 (**3**): 037501. DOI: 10.1088/1674-1056/28/3/037501

Temperature-dependent interlayer exchange coupling strength in synthetic antiferromagnetic$[Pt/Co]_2/Ru/[Co/Pt]_4$ multilayers

Yong Li(李勇), Xiangjun Jin(金香君), Pengfei Pan(潘鹏飞), Fu Nan Tan, Wen Siang Lew, Fusheng Ma(马付胜)
Chin. Phys. B, 2018, 27 (**12**): 127502. DOI: 10.1088/1674-1056/27/12/127502

RAPID COMMUNICATION

Characterization of interlayer coupling in YIG/Py bilayer using polarized neutron reflectometry

He Bai(白鹤)[1,2], Wei He(何为)[3], Dan Liu(刘丹)[4], Jialiang Li(李嘉亮)[1,2], Xiao Deng(邓霄)[2,5], Yuan Sun(孙远)[1,2], Songwen Xiao(肖松文)[1,2], Sheng Cheng(成晟)[1,2], Xiaozhi Zhan(詹晓芝)[1,2], Jianwang Cai(蔡建旺)[3], and Tao Zhu(朱涛)[2,3,6,†]

[1] *Institute of High Energy Physics, Chinese Academy of Sciences, Beijing* 100049, *China*
[2] *Spallation Neutron Source Science Center, Dongguan* 523803, *China*
[3] *Beijing National Laboratory for Condensed Matter Physics and Institute of Physics, Chinese Academy of Sciences, Beijing* 100190, *China*
[4] *Department of Physics, Beijing Technology and Business University, Beijing* 100048, *China*
[5] *University of Science and Technology Beijing, Beijing* 100083, *China*
[6] *Songshan Lake Material Laboratory, Dongguan* 523808, *China*

(Received 9 July 2025; revised manuscript received 9 July 2025; accepted manuscript online 23 July 2025)

The complex interplay of magnetic interactions at the yttrium iron garnet (YIG)/ferromagnet interface is important for spintronic and magnonic devices. In this study, we present a comprehensive investigation of the interlayer coupling and switching mechanisms in YIG/Py (permalloy) heterostructures based on gadolinium gallium garnet (GGG) and SiO_2 substrates. We observe antiferromagnetic interlayer coupling between Py and YIG on SiO_2 substrates, whereas ferromagnetic interlayer coupling is observed on GGG substrates. Using polarized neutron reflectometry with depth- and element-resolved measurements, we obtain an in-depth understanding of the magnetic interactions between the YIG and Py layers. We demonstrate that polycrystalline YIG gives rise to antiferromagnetic interlayer coupling. This work provides valuable insights into designing and controlling magnetic coupling in hybrid structures for spintronic applications.

Keywords: interlayer coupling, polarized neutron reflectivity, yttrium iron garnets

PACS: 75.70.–i, 75.30.Et, 61.05.fj

DOI: 10.1088/1674-1056/adf31e **CSTR:** 32038.14.CPB.adf31e

1. Introduction

The transport of spin information has been studied in various materials, including metals,[1,2] semiconductors,[3] and graphene.[4] In these materials, spins are transported by conduction electron diffusion. Meanwhile, magnetic insulators can transfer spin information through the diffusion of non-equilibrium magnons, which are the quanta of spin-wave excitations in magnetically ordered materials.[5] $Y_3Fe_5O_{12}$ (yttrium iron garnet, YIG) is especially important in magnon dynamics and manipulation due to its exceptionally low damping constant ($\alpha \approx 10^{-5}$), notably large magnon decay length, and extended magnon lifetimes.[6,7] The unique magnetic properties of YIG thin films give them broad application potential in magnonic devices.[8–11] For instance, Yu *et al.*[12] investigated the magnon transport behavior in multilayers comprising YIG and other materials, paving the way for novel magnon-based devices.[13] Han's group[14,15] investigated the magnon-mediated spin–orbit torque (SOT) in YIG-based heterostructures using spin-torque ferromagnetic resonance (ST-FMR) measurements. Zhang *et al.*[16] developed spin-wave transmission devices based on detect/receive microstrip antennas, employing the spin pumping method.

Recently, interest in another YIG heterostructure with a ferromagnetic (FM) layer has increased due to the magnetization interactions mediated by the interlayer coupling between two adjacent nanomagnetic layers. The interlayer magnon–magnon coupling has been detected in such a hybrid structure. Klingler *et al.*[17] reported antiferromagnetic (AFM) interlayer coupling between YIG and Co while demonstrating efficient perpendicular standing spin waves (PSSW) in the YIG layer. Li *et al.*[18] observed coherent spin pumping in a strongly antiferromagnetically coupled YIG/Py bilayer. Zhang *et al.*[13] formulated a strong-coupling theory for PSSW in the YIG/Py bilayer. Sheng *et al.*[12] detected nonlinear interlayer magnon interactions in a hybrid magnetic nanostructure (YIG/CoFeB) via nonlocal spin pumping. These findings suggest that coupling between layered structures, which can be controlled by manipulating interlayer interactions, has great potential for YIG-based magnonic devices. Uncovering the effective manipulation mechanism of magnon transmission is vital.

In addition to magnon–magnon coupling, the interlayer exchange interactions in these hybrid structures enable additional magnonic applications, such as magnon spin valves. The transmission efficiency of magnons propagating through

†Corresponding author. E-mail: tzhu@iphy.ac.cn

© 2025 Chinese Physical Society and IOP Publishing Ltd. All rights, including for text and data mining, AI training, and similar technologies, are reserved.

a magnon spin valve is tuned by the parallel or antiparallel orientation of the magnetization of the two magnetic layers. YIG-based multilayers have also been used to develop magnon spin valves. Wang *et al.*[19] achieved pronounced bistable switching in a 1 μm wide magnonic conduit (YIG strip) under an external RF drive. The system is characterized by two stable magnonic states, defined as low- and high-amplitude spin waves. Fan *et al.*[20] observed antiferromagnetic interlayer coupling between YIG/Py bilayer films on silicon and GGG substrates, respectively. They fabricated a magnon spin valve with an on–off ratio of approximately 130% using a YIG/Py bilayer with antiferromagnetic interlayer coupling. Quarterman *et al.*[21] found that YIG and Py exhibit an antiferromagnetic arrangement on a silicon substrate, while YIG and Py exhibit a ferromagnetic arrangement on a GGG substrate.

For practical device applications, spin-valve structures grown on silicon substrates are preferred. However, much remains unknown about the contradictory magnetic configurations reported above, particularly regarding the origin of this antiparallel exchange interaction and its applicability to other FM layers or substrates. In this study, we used polarized neutron reflectometry (PNR) to examine the magnetic states of the YIG/Py system. Our results revealed differences in the arrangement of magnetic moments on various substrates. We found that YIG/Py on SiO_2 substrates exhibits antiferromagnetic interlayer coupling, while YIG/Py on GGG substrates exhibits ferromagnetic interlayer coupling. Through the combination of x-ray diffraction and scanning transmission electron microscopy, we concluded that the polycrystalline YIG on the SiO_2 substrate is the main cause of the antiferromagnetic interlayer coupling.

2. Methods

Sample preparation The YIG films were epitaxially grown on (111)-oriented $Gd_3Ga_5O_{12}$ (GGG) single-crystal substrates and silicon substrates, respectively. The base pressure of the sputtering system was better than 4×10^{-6} Pa, and the working gas was high-purity Ar (99.999%) at 1.0 Pa. After deposition, all films were annealed at 800 °C for 2 h in a quartz tube with a pure oxygen pressure of 500 Pa under an oxygen flow rate of 45 sccm. Then the samples were rapidly cooled to room temperature by quickly moving the furnace away from the sample zone of the quartz tube to suppress strain relaxation. After annealing, a $Ni_{80}Fe_{20}$ (Py) layer was grown on the SiO_2/YIG and GGG/YIG samples inside the magnetron sputtering chamber, using DC sputtering with the Ar pressure of 0.5 Pa at room temperature. A final 5 nm-thick SiO_2 layer was deposited to protect the metal films against oxidation.

Sample characterizations The θ–2θ scans were performed on a high-resolution x-ray diffractometer (XRD, Bruker D8-Discover diffractometer) with Cu $K\alpha$ radiation. High-resolution transmission electron microscopy (HRTEM) images were obtained using an FEI Tecnai G2 F20 field emission transmission electron microscope (FETEM). The cross-sectional specimens of the SiO_2/YIG/Py and GGG/YIG/Py samples were prepared by focused ion beam lift-out using an FEI Scios 2. Before lift-out, protective layers of sputtered tungsten were applied to the surface of the thin film. Rough milling steps were performed with 30 keV Ga^+ ions, and the final thinning of the samples was performed at 5 keV to reduce surface damage. Both high-angle annular-dark-field (HAADF) and annular bright field (ABF) imaging were performed in the scanning mode. Elemental-specific EELS mappings were performed at the Y *L*-, Fe *L*-, O *L*-, Si *L*-, and Ni *L*-edges in the regions of interest. All structural characterizations were performed at room temperature. Magnetic properties were studied using a vibrating sample magnetometer (VSM, Model 4 HF, MicroSense LLC).

PNR measurement Polarized neutron reflectometry (PNR) was carried out at the multipurpose reflectometer (MR) beamline of the Chinese Spallation Neutron Source (CSNS). The substrate size was 10×10 mm^2. The room temperature neutron reflectivity curves were recorded at room temperature as a function of momentum transfer $Q_z = 4\pi \sin\theta/\lambda$, where λ is the neutron wavelength and θ is the incident angle between the neutron beam and the film plane. To access a broad momentum transfer range, reflected neutrons were collected at different incident angles. Both R^{++} and R^{--} were recorded when neutrons with spins parallel or antiparallel to the applied field (corresponding to spin-up and spin-down neutrons), respectively. PNR data were fitted to a model (including the layer thickness and chemical roughness) that was obtained by XRR fitting using the software GenX.

3. Results and discussion

First, we deposited 40-nm YIG and 20-nm Py layers on GGG and Si/SiO_2 substrates, with a 5-nm protective SiO_2 layer on top. Figures 1(a) and 1(b) show the XRD $2\theta/\omega$ patterns of the YIG films on SiO_2 and GGG substrates, respectively. Both XRD patterns exhibit a distinct Py peak along the (111) direction. From Fig. 1(a), it can be clearly observed that the YIG film exhibits a polycrystalline nature with large (400), (420), and (422) reflections. Meanwhile, the XRD pattern in Fig. 1(c) shows a very strong (444) GGG peak and a relatively weak additional peak on the right shoulder, corresponding to the (444) YIG, along with pronounced Laue oscillations. The corresponding rocking curve of the (444) YIG peak has a very small full width at half maximum of approximately 0.02°, as shown in the inset of Fig. 1(c). These results indicate the high single-crystalline quality of the YIG films and their excellent orientation along the (111) crystallographic direction. Based on these XRD results, we can conclude that the YIG grown on

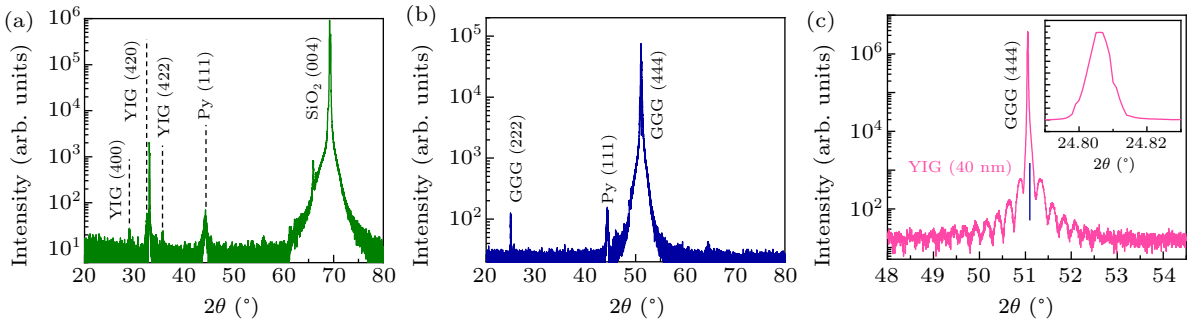


Fig. 1. X-ray diffraction $2\theta/\omega$ scans of 40 nm YIG films grown on (a) SiO_2 substrate and (b) GGG substrate. (c) XRD pattern in the range of [48°, 54°]. The vertical short line indicates the position of the YIG (444) peak. Inset: rocking curve of the YIG (444) reflection.

a GGG substrate demonstrates high-quality epitaxial growth, whereas the YIG grown on a SiO_2 substrate exhibits a polycrystalline nature.

Figure 2 shows the corresponding HAADF scanning transmission electron microscopy (STEM) cross-sectional images of the GGG/YIG/Py and SiO_2/YIG/Py samples. Energy-dispersive x-ray spectroscopy profiles are used to probe element diffusion (see Fig. S1 in the supplementary materials). No obvious interdiffusion between the layers is observed. The images also illustrate the high uniformity of the bilayer samples, which are free of observable defects, and show that the thickness of each layer is consistent with the designed thickness. As shown in Fig. 2(a), a sharp interface between the YIG and GGG is identified, and it is clearly evident that the YIG is epitaxially grown on the GGG substrate. However, the SiO_2/YIG interface, as shown in Fig. 2(b), is rather obscure, indicative of an interdiffusion region across the SiO_2/YIG interface. The YIG surface termination on the GGG substrate comprises a plane of visible Fe and Y atoms and invisible O atoms. This results in an interface layer that connects sharply to the Py layer. In contrast, the YIG/Py interface on the SiO_2 substrate exhibits a blurred interface. The indistinct interface may arise from excessive roughness or elemental diffusion. STEM further confirms well-oriented lattices with a sharp interface between the epitaxial YIG and the Py layer, and an obscure interface between the polycrystalline YIG and the Py layer.

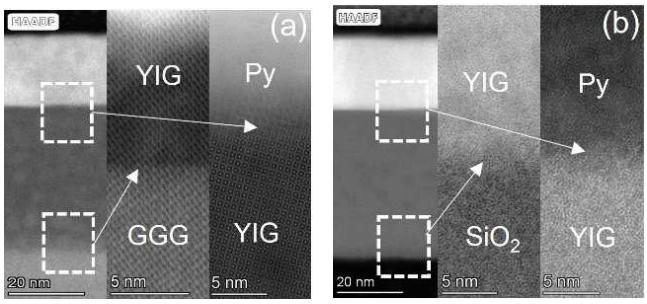


Fig. 2. Cross-sectional HRTEM images of the substrate/YIG and YIG/Py interfaces on (a) GGG and (b) SiO_2 substrates.

To characterize the arrangement of magnetic moments in the hybrid structure, we collected magnetization data at room temperature with magnetic fields applied within the sample plane. Figure 3(a) illustrates the schematic of the YIG/Py/SiO_2 grown on GGG and SiO_2 substrates. Figures 3(b)–3(c) and 3(e)–3(f) show the M–H curves of the GGG-based and SiO_2-based samples, respectively. The inset in Fig. 3(b) shows the M–H loops of the GGG/YIG(40)/Py(3) and the GGG/YIG(40) control sample in the high-field region (the capping SiO_2 is omitted). Reducing the range of the external field reveals that the M_s of GGG/YIG(40)/Py(3) is slightly larger than that of GGG/YIG(40), though its coercivity is slightly smaller. No AFM interlayer coupling between the YIG and Py layers was observed. To further validate this conclusion, GGG/YIG(40)/Py(20) was also measured, as shown in Fig. 3(c). From the high-field region in the inset, no clear evidence of interfacial coupling can be obtained. In the low-field region, the magnetization of YIG(40)/Py(20) saturates at 10 Oe. As the field decreases, a gradual reduction in magnetization begins at 5 Oe. When the magnetic field reaches 0 Oe, the net magnetic moment of YIG(40)/Py(20) matches that of YIG(40), indicating that the decrease in magnetization occurs only in the Py layer, without antiparallel alignment to the external field. As the magnetic field continues to decrease, the magnetization of YIG(40)/Py(20) also decreases, indicating that the YIG magnetization begins to decrease, reaching zero at approximately −0.65 Oe. With the application of a stronger negative field, the magnetization of YIG(40)/Py(20) reverses direction, suggesting that the YIG magnetization aligns with the negative field. When the magnetic field reaches −1.5 Oe, the magnetization of YIG(40)/Py(20) matches that of YIG(40), indicating that the YIG magnetization has completely reversed to align with the negative field, while the Py magnetization has not yet. As the magnetic field increases further, the Py magnetization begins to reverse. By −5 Oe, the Py magnetization has completely reversed. At this point, the magnetization of YIG(40)/Py(20) is equal to the sum of the magnetizations of YIG(40) and Py(20). Figure S2(a) shows the M–H curves of the control GGG/YIG(100)/Py(20) and GGG/YIG(100) samples, respectively. Similarly, no evidence of AFM interlayer coupling between the YIG and Py layers is observed.

Next, we examine the M–H curves of the SiO_2-based samples. Figure 3(d) shows the M–H curves of the 40-nm and 100-nm YIG layers and the 20-nm Py layer on SiO_2 substrates. These curves typically exhibit easy-axis hysteresis loops with a low coercive field and a square switching shape. As shown by previously reported magnetization results,[20] the M_s of YIG on a GGG substrate is slightly larger than that on a SiO_2 substrate. The larger H_c of polycrystalline YIG films may be due to their small grain size. Figure 3(e) shows the results for the SiO_2/YIG(40)/Py(3) sample and the control sample SiO_2/YIG(40)/MgO(3)/Py(3). Similarly, no AFM interlayer coupling between YIG and Py was observed due to the thinness of the Py film. Figure 3(f) demonstrates the M–H curve of the SiO_2/YIG(40)/Py(20) sample, which exhibits segmented switching features. As the external field gradually decreases from positive saturation, the M_s of SiO_2/YIG(40)/Py(20) also decreases. When the magnetic field reaches 0 Oe, the net magnetic moment of SiO_2/YIG(40)/Py(20) equals the difference in magnetization between the Py(20) and YIG(40) layers. This suggests that the YIG magnetization is oriented negatively and that AFM interlayer coupling may exist between these two layers. After the magnetization switches polarity sharply near $H = 0$ Oe, the Py magnetization reverses completely. The M_s of SiO_2/YIG(40)/Py(20) remains equal to the difference in M_s between the Py(20) and YIG(40) layers, meaning that the YIG magnetization also reverses and points in a positive orientation to maintain its antiparallel alignment. Subsequently, the YIG magnetization gradually aligns with the external field in the negative direction, reaching saturation at around $H = 1.2$ kOe.

To investigate the underlying mechanisms of the observed AFM interlayer coupling, we fabricated a control sample consisting of SiO_2/YIG(40)/MgO(3)/Py(20). In this sample, the MgO layer acts as a spacer, preventing direct exchange coupling between the YIG and Py layers. Unlike the SiO_2/YIG(40)/Py(20) sample, this control sample's M–H curve exhibits complete switching near $H = 0$ Oe. This indicates that the observed coupling is due to an exchange interaction rather than a dipolar field. To further elucidate the mechanism, we changed the YIG layer thickness to 100 nm. The results are shown in Fig. S2(b). The data exhibit a similar trend to those in Fig. 3(f), except for the different saturation field and M_s value at zero field. By comparing the magnetization of the single layer in Fig. 3(d), we found that the M_s of SiO_2/YIG(100)/Py(20) at zero field is equal to that of SiO_2/Py(20). This suggests that the YIG magnetization is not oriented negatively but instead decreases in magnitude. This may be attributed to the increased YIG thickness, which dominates the moment and results in weak antiparallel coupling between YIG and Py. This interpretation is confirmed by the saturation field. The saturation field of SiO_2/YIG(100)/Py(20) is much smaller than that of SiO_2/YIG(40)/Py(20). The former saturates around 600 Oe, while the latter saturates around 1.2 kOe, approximately half that value. For comparison, Fig. S2(b) also shows the M–H curve of the control sample, SiO_2/YIG(100)/MgO(3)/Py(20). As anticipated, the MgO spacer layer prevents coupling between the two layers, exhibiting full switching near $H = 0$ Oe with more distinct square-shaped corners, originating from the thicker YIG films.

To directly probe the magnetization of these samples, we use PNR to measure the depth profile of their chemical composition and magnetization.[8] Figure 4(a) shows a typical set of PNR data obtained from the GGG/YIG(40)/Py(20)/SiO_2(5)

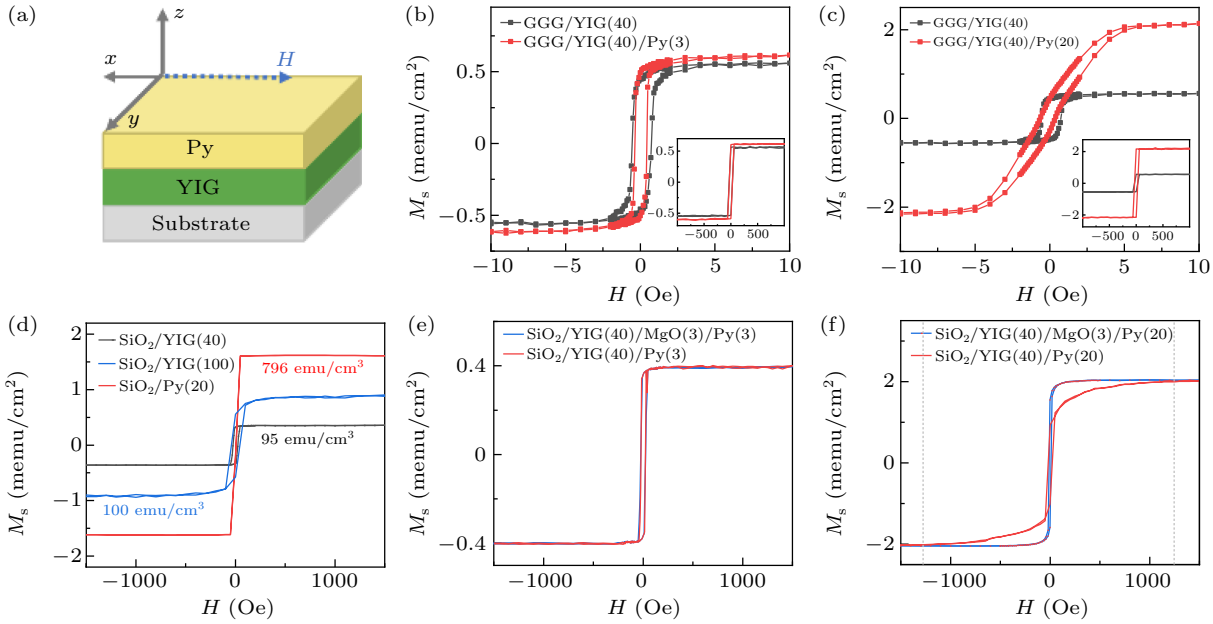


Fig. 3. (a) Schematic of the YIG/Py bilayer on different substrates. (b)–(c) M–H curves of GGG/YIG/Py/SiO_2 with varying layer thicknesses. (d) M–H curves of single layers on a SiO_2 substrate. (e)–(f) M–H curves of SiO_2/YIG/Py/SiO_2 with varying layer thicknesses.

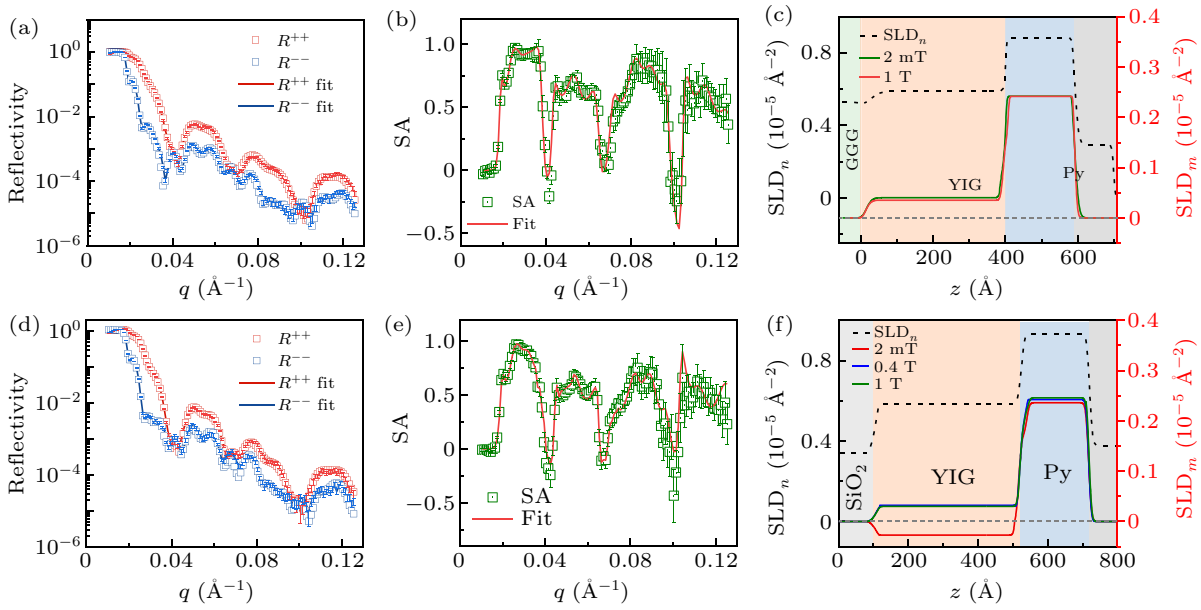


Fig. 4. PNR measurements of GGG/YIG(40)/Py(20)/SiO_2(5) and SiO_2/SiO_2(10)/YIG(40)/Py(20)/SiO_2(5). (a) and (d) PNR curves measured at $H = 2$ mT. Symbols represent the experimental data, while solid lines show the fitted curves. (b) and (e) Spin-asymmetry (SA) curves, including both experimental and fitted data. (c) and (f) Fitted nuclear and magnetic SLD (SLD$_n$ and SLD$_m$) profiles.

sample under an external magnetic field of 2 mT, which was reached by first saturating at 1 T and then lowering the field. As described in Section 2, the solid lines represent theoretical reflectivity curves generated from the scattering length density (SLD) depth profiles shown in Fig. 4(c). The spin-asymmetry (SA), defined as $\mathrm{SA} = (R^{++} - R^{-})/(R^{++} + R^{-})$, is highly sensitive to the film magnetization, as shown in Fig. 4(b). The nuclear and magnetic SLD (SLD$_n$ and SLD$_m$) are directly proportional to the in-plane magnetization and chemical composition as a function of depth from the sample surface. The PNR data under 1 T are provided in the supplementary material. The SLD profiles reveal sharp interfaces at the GGG/YIG and YIG/Py boundaries. The nuclear and magnetic SLDs are in close agreement with the expected values.[22–24] Under both high and low fields, we observe only minor changes in the magnetic depth profile, and a clear absence of antiparallel coupling. We then performed PNR at 2 mT, 0.4 T, and 1 T on a SiO_2/SiO_2(10)/YIG(40)/Py(20)/SiO_2(5) sample. The PNR and SA data under 2 mT are shown in Figs. 4(d) and 4(e), and the data for 0.4 T and 1 T are presented in the supplementary material. The associated best-fit depth profiles are shown in Fig. 4(f). Both SLD$_n$ and SLD$_m$ for YIG are consistent with bulk values.[21] Specifically, under high fields (0.4 T and 1 T), the YIG and Py layers align parallel to the applied field. Under the low field (2 mT), the Py magnetization remains nearly unchanged, while the magnetization of the YIG is almost completely antiparallel to the external magnetic field (i.e., aligned with the Py magnetization direction). The PNR results, including the magnetic field at which YIG magnetization fully reverses, as well as the magnitude of the magnetic moment at this field, agree well with the M–H curve shown in Fig. 3(f).

Table 1. Summary of exchange-coupling configuration in YIG/Py bilayers.

Sample	Orientation	Coupling	Note
GGG/YIG/Co[17]	(111)	AFM	Piranha etch
GGG/YIG/Py[18]	(111)	AFM	ion milling
GGG/Pt/YIG/Py[25]	(110)	AFM	Pt as seed layer
GGG/YIG/Py[21]	(111)	FM	–
GGG/YIG/Py	(111)	FM	–
SiO_2/(Pt)/YIG/Py[20]	polycrystalline	AFM	Pt as seed layer
SiO_2/YIG/Py	polycrystalline	AFM	–

As summarized in Table 1, previous results and our study indicate that AFM interlayer coupling is usually observed between YIG and Py on a SiO_2 substrate. For samples on GGG substrates, however, both FM and AFM interlayer coupling are possible. There are several possible reasons. First, the polycrystalline nature of YIG has a significant impact. YIG grown on a GGG substrate is a high-quality single crystal, whereas it is polycrystalline on a SiO_2 substrate. The (420) and (400) orientations of YIG are the most likely origins of antiparallel magnetic coupling in SiO_2-based samples, as well as grain boundaries and variations in YIG surface orientations.[21] This agrees with our XRD results, in which multiple peaks from different crystal orientations were observed.

Second, the surface morphology and termination may lead to AFM interlayer coupling. In Refs. [17,18], YIG was chemically and physically etched before Py deposition: by Piranha solution and ion milling, respectively. Thus, the surface roughness and elemental concentration may have been modified during the etching process. Specifically, the (110)-oriented GGG/YIG/Py in Ref. [25] supports AFM interlayer coupling between YIG and Py without any etching treatment. We speculate that this may be due to different surface termi-

nations induced by different orientations. The relative surface concentrations of Y, Fe, and O are different for (110)- and (111)-substrates. AFM interlayer coupling is an energetically favorable magnetic state for tetrahedral Fe-terminated YIG/Py, while the octahedral Fe-terminated YIG/Py interface can exhibit either AFM or FM interlayer coupling without a particular preference.[26] Thus, ion milling of the YIG surface by Ar^+ leads to the dominant role of tetrahedral Fe in the surface termination, while simultaneously removing the reconstructed YIG layer caused by Fe deficiency.[26] We believe that the combined effect of these two factors may result in AFM interlayer coupling in Refs. [17,18].

In our study, we used the same preparation procedures as Ref. [21] without any surface treatment. This preserved the initial elemental concentrations of both tetrahedral and octahedral Fe atoms, as well as the possible Fe deficiency, which suppresses the AFM interlayer coupling between YIG and Py. These observations reinforce the idea that interlayer coupling is determined by a complex interplay of several factors. Finally, for SiO_2-based samples, the polycrystalline property is responsible for AFM interlayer coupling, while interface details also contribute. Although randomly oriented crystal grains may cause a mixture of tetrahedral and octahedral Fe at the YIG surface termination, the presence of disorder or grain boundaries at the YIG interface may give rise to AFM interlayer coupling.[21] The details of surface morphology and termination can lead to antiparallel exchange coupling; however, this requires further systematic study.

4. Conclusion

In summary, we carried out a detailed characterization and analysis of interlayer coupling in GGG- and SiO_2-based YIG/FM heterostructures. We found that Py and YIG on a SiO_2 substrate demonstrate AFM interlayer coupling, whereas the coupling on a GGG substrate is ferromagnetic, as evidenced by both magnetic hysteresis loops and PNR measurements. XRD results revealed that YIG on SiO_2 substrates exhibits a polycrystalline structure with multiple orientations, such as (400), (420), and (422), which can account for the AFM interlayer coupling. The coexistence of grain boundaries and varied surface orientations may further induce magnetic frustration and reconstruction, contributing to the observed AFM coupling. For GGG-based samples, YIG surface termination appears to play a dominant role. Given the surface sensitivity of interfacial exchange coupling, effects related to surface termination or microstructure-induced frustration remain plausible explanations, and further investigation is warranted.

Data availability statement

The data supporting the findings of this study are openly available in the Science Data Bank at the following link: https://doi.org/10.57760/sciencedb.j00113.00270.

Acknowledgments

This work was supported by the National Key Basic Research Program of China (Grant Nos. 2021YFA1400300 and 2023YFA1610400), the National Natural Science Foundation of China (Grant Nos. 12204268, 52371169, 52130103, and U22A20263), the Guangdong Basic and Applied Basic Research Foundation (Grant No. 2023B1515120015), and the Open Research Fund of Songshan Lake Materials Laboratory (Grant No. 2022SLABFN13). PNR experiments were conducted at the Beamline MR of the Chinese Spallation Neutron Source.

References

[1] Huang S Y, Fan X, Qu D, Chen Y P, Wang W G, Wu J, Chen T Y, Xiao J Q and Chien C L 2012 *Phys. Rev. Lett.* **109** 107204
[2] Miao B F, Huang S Y, Qu D and Chien C L 2013 *Phys. Rev. Lett.* **111** 066602
[3] Jaworski C M, Yang J, Mack S, Awschalom D D, Heremans J P and Myers R C 2010 *Nat. Mater.* **9** 898
[4] Singh S, Katoch J, Zhu T, Meng K Y, Liu T, Brangham J T, Yang F, Flatte M E and Kawakami R K 2017 *Phys. Rev. Lett.* **118** 187201
[5] Chumak A V, Vasyuchka V I, Serga A A and Hillebrands B 2015 *Nat. Phys.* **11** 453
[6] Soumah L, Beaulieu N, Qassym L, Carretero C, Jacquet E, Lebourgeois R, Youssef J B, Bortolotti P, Cros V and Anane A 2018 *Nat. Commun.* **9** 3355
[7] Wesenberg D, Liu T, Balzar D, Wu M and Zink B L 2017 *Nat. Phys.* **13** 987
[8] Bai H, Zhan X Z, Li G, Su J, Zhu Z Z, Zhang Y, Zhu T and Cai J W 2019 *Appl. Phys. Lett.* **115** 182401
[9] Nakayama H, Althammer M, Chen Y T, Uchida K, Kajiwara Y, Kikuchi D, Ohtani T, Geprags S, Opel M, Takahashi S, Gross R, Bauer G E, Goennenwein S T and Saitoh E 2013 *Phys. Rev. Lett.* **110** 206601
[10] Avci C O, Quindeau A, Pai C F, Mann M, Caretta L, Tang A S, Onbasli M C, Ross C A and Beach G S 2017 *Nat. Mater.* **16** 309
[11] Bai H, Li J, Ke J, Guo Q, Zhu Z, Guo Y, Deng X, Liu D, Cai J and Zhu T 2024 *Adv. Electron. Mater.* **10** 2300785
[12] Sheng L, Elyasi M, Chen J, He W, Wang Y, Wang H, Feng H, Zhang Y, Medlej I, Liu S, Jiang W, Han X, Yu D, Ansermet J P, Bauer G E W and Yu H 2023 *Phys. Rev. Lett.* **130** 046701
[13] Zhang Z, Yang H, Wang Z, Cao Y and Yan P 2021 *Phys. Rev. B* **103** 104420
[14] Dong J, Cheng C, Wei J, Xu H, Zhang Y, Wang Y, Zhu Z, Li L, Wu H, Yu G and Han X 2023 *Appl. Phys. Lett.* **122** 122401
[15] Guo C Y, Wan C H, Wang X, Fang C, Tang P, Kong W J, Zhao M K, Jiang L N, Tao B S, Yu G Q and Han X F 2018 *Phys. Rev. B* **98** 134426
[16] Rao Y H, Zhang H W, Yang Q H, Zhang D N, Jin L C, Ma B and Wu Y J 2018 *Chin. Phys. B* **27** 086701
[17] Klingler S, Amin V, Geprägs S, Ganzhorn K, Maier-Flaig H, Althammer M, Huebl H, Gross R, McMichael R D, Stiles M D, Goennenwein S T B and Weiler M 2018 *Phys. Rev. Lett.* **120** 127201
[18] Li Y, Cao W, Amin V P, Zhang Z, Gibbons J, Sklenar J, Pearson J, Haney P M, Stiles M D, Bailey W E, Novosad V, Hoffmann A and Zhang W 2020 *Phys. Rev. Lett.* **124** 117202
[19] Wang Q, Verba R, Davidkova K, Heinz B, Tian S, Rao Y, Guo M, Guo X, Dubs C, Pirro P and Chumak A V 2024 *Nat. Commun.* **15** 7577

[20] Fan Y, Quarterman P, Finley J, Han J, Zhang P, Hou J T, Stiles M D, Grutter A J and Liu L 2020 *Phys. Rev. Appl.* **13** 061002
[21] Quarterman P, Fan Y, Chen Z, Jensen C J, Chopdekar R V, Gilbert D A, Holtz M E, Stiles M D, Borchers J A, Liu K, Liu L and Grutter A J 2022 *Phys. Rev. Mater.* **6** 094418
[22] Liu Q B, Meng K K, Xu Z D, Zhu T, Xu X G, Miao J and Jiang Y 2020 *Phys. Rev. B* **101** 174431
[23] Roos M J, Quarterman P, Ding J, Wu M, Kirby B J and Zink B L 2022 *Phys. Rev. Mater.* **6** 034401
[24] Suturin S M, Korovin A M, Bursian V E, Lutsev L V, Bourobina V, Yakovlev N L, Montecchi M, Pasquali L, Ukleev V, Vorobiev A, Devishvili A and Sokolov N S 2018 *Phys. Rev. Mater.* **2** 104404
[25] Fan Y, Finley J, Han J, Holtz M E, Quarterman P, Zhang P, Safi T S, Hou J T, Grutter A J and Liu L 2021 *Adv. Mater.* **33** 2008555
[26] Qian J, Li Y, Jiang Z, Busch R, Ni H C, Lo T H, Hoffmann A, Schleife A and Zuo J M 2024 arXiv:2402.14553 [cond-mat.mtrl-sci]